Journal of Materials Processing Tech. 258 (2018) 138–143

Contents lists available at ScienceDirect

Journal of Materials Processing Tech.

journal homepage: www.elsevier.com/locate/jmatprotec

Dendritic coarsening model for rapid solidification of Ni-superalloy via electrospark deposition

Pablo D. Enrique[a,*], Zhen Jiao[b], Norman Y. Zhou[a], Ehsan Toyserkani[a]

[a] University of Waterloo, 200 University Ave W, Waterloo, Ontario, N2L 3G1, Canada
[b] Huys Industries Ltd., 175 Toryork Drive, Unit 35 Weston, Ontario, M9L 1X9, Canada

ARTICLE INFO

Keywords:
Electrospark deposition
Microstructure
Cellular dendritic subgrain
Nickel superalloy
Microhardness

ABSTRACT

Control of splat thickness in an electrospark deposition (ESD) process can be used to improve the mechanical properties of deposited Inconel 718. The lower cooling rates of thicker deposition splats obtained through higher energy ESD parameters result in greater subgrain coarsening and lower microhardness. A subgrain growth model and Hall-Petch relationship are used to quantify the extent of subgrain coarsening and the influence of splat thickness on hardness, with a 4.5 times reduction in splat thickness achieving a 20% increase in microhardness.

1. Introduction

ESD has found several applications in wear or corrosion resistant coatings and as a repair technique for cracked and pitted components. Sartwell et al. (2006) achieved successful mechanical property and dimension restoration for stainless steel, Inconel and nickel-copper alloy components, the assessment of which was based on porosity, microhardness, wear resistance, tensile and fatigue testing, and surface finish analysis. These applications benefit from a deposited material with properties equivalent to – or better – than the base metal, which can be achieved through a finer grain structure. The Hall-Petch relationship indicates that smaller grain sizes result in a greater yield strength, alongside other improvements to ultimate tensile strength, hardness and wear resistance (Russell and Lee, 2005).

Nanoscale grains have been reported to form in various electrospark deposition (ESD) processed materials including aluminum-zirconium alloys (Brochu and Portillo, 2013) and Fe_2B (Wei et al., 2017). These small grain sizes are attributed to the short pulse duration of the ESD process, allowing for rapid solidification and cooling of the material between each deposition. The use of ESD to restore oxidation resistant coatings by Farhat and Brochu (2012), found that the performance of the repaired coating was improved due to the fine grain structure of the deposited material, which allowed for improved diffusion along the grain boundaries. Improved tribological properties (increased wear resistance) of nanoscale structured ESD WC-Co coatings have also been reported in the literature (Wang et al., 2010). The improved properties were directly attributed to the nanostructured coating, which resulted in increased hardness and the formation of lubricating oxides.

Ruan et al. (2016) showed that decreasing dendrite diameter and secondary dendrite arm spacing both resulted in a microhardness increase, analogous to the Hall-Petch relationship. The presence of cellular dendritic structures in ESD processed materials have been reported for nickel based superalloys by Ebrahimnia et al. (2014), which formed parallel to the ESD growth direction with submicron diameters. Other rapid solidification processes exhibit similar cellular dendritic structures for nickel-based superalloys, including laser powder bed additive manufacturing of Hastelloy X (Saarimäki et al., 2016). In this process, cellular dendritic structures with primary arm diameters less than 1 μm and no secondary arm formation were attributed to high cooling rates. Although the presence of subgrain structures is well documented, the ability to control the dendritic subgrain diameter in an ESD process is beneficial for optimizing mechanical properties. A model based on a subgrain growth mechanism is developed and used to relate the deposition splat thickness with the cellular dendritic subgrain diameter, as well as describing the effect of splat thickness on hardness in ESD processed Inconel 718.

2. Experimental methods

An Inconel 718 solution-annealed sheet obtained from McMaster-Carr was used as the substrate material for the ESD process. The substrate surface was 6 cm^2 and the substrate thickness was 3.2 mm, with the supplier provided chemical composition listed in Table 1. Inconel 718 solution-treated electrodes obtained from AlloyShop with a 3.2 mm diameter were used.

The deposition process was performed using a Huys Industries ESD

* Corresponding author.
E-mail address: pdenriqu@uwaterloo.ca (P.D. Enrique).

https://doi.org/10.1016/j.jmatprotec.2018.03.023
Received 13 December 2017; Received in revised form 23 March 2018; Accepted 25 March 2018
Available online 27 March 2018
0924-0136/

Table 1
Inconel 718 Substrate Composition (wt%).

Ni	Fe	Cr	Nb	Mo	Ti	Co	Al	C	Mn	Si	Cu
53.5	17.8	18.5	5.1	2.9	0.9	0.2	0.6	0.03	0.09	0.08	0.13

Table 2
ESD Process Window.

Parameter	Value(s)
Pulse Frequency (Hz)	170
Voltage (V)	50, 100, 120
Capacitance (μF)	80, 100, 120

machine. A process window varying several process parameters was used to obtain depositions with low and high energy parameters. Due to the effect of capacitance and voltage on the input energy of the ESD process, several voltage and capacitance values were used while maintaining constant pulse frequency. These parameters are summarized in Table 2. Argon cover gas was used at a flow rate of 10 L/min and the material was deposited in a bidirectional raster scan pattern for each sample. Deposition time was kept constant by manually controlling the electrode travelling speed, with a single pass on a 1 cm^2 area requiring 20 s of coating time. A total of 10 passes were performed for each sample, with a 10 s peening step using a hand-held motorized tool after each pass. The use of a peening step leads to a reduction in surface roughness, improving the uniformity of subsequently deposited layers.

One sample was created for each process parameter and the samples were cross-sectioned and mounted in a conductive resin, after which they were subjected to a series of grinding (400, 600, 800 and 1200 grit) and diamond polishing (6, 3, 1 μm) steps. The samples were then etched by immersion using inverted glyceregia ($HCl:HNO_3$:Glycerol in a 5:1:1 ratio) for 1.5 and 3.5 min (Vander Voort, 1998), with a shorter time required to etch the deposited material and a longer time required to etch the substrate.

Analysis of the prepared samples was performed on a JEOL JSM-6460 scanning electron microscope (SEM) with an Oxford Instruments INCAx-sight EDX attachment and an Oxford BX51M optical microscope (OM). Subgrain diameter measurements were performed using the intercept method for grain size determination (ASTM E112-13), modified to account for the cellular dendritic shape. A line of known length was drawn perpendicular to the subgrain growth direction, and the length was divided by the number of intersected subgrains to get the average subgrain diameter. Hardness measurements were made using a load of 0.1 kgf on a Wolpert Wilson 402 MVD micro Vickers hardness tester. Indentations on the boundary between deposition splats were avoided.

3. Results and discussion

Microscopic analysis of ESD deposited Inconel 718 after etching shows a series of individually deposited splats with varying thicknesses that stack to form the coating. Higher voltage and capacitance parameters result in higher deposition rates and poorer coating quality, as seen in Fig. 1a, while lower parameters result in favourable coatings with no significant voids or cracks (Fig. 1b).

The ESD process deposits material through a series of short electrical pulses determined by the frequency parameter, with each of these pulses depositing a single splat on the substrate surface. The rapid cooling rates associated with ESD allow for the deposited material to solidify prior to the deposition of a subsequent splat, forming the layered microstructure in Fig. 1. As can be seen by the uneven substrate-deposition interface, some of the substrate is melted during the deposition of the first layer. This can also be expected with subsequent depositions, where a portion of the previously deposited material is re-melted.

Higher magnification images of the deposited layers show large regions with submicron cellular dendritic subgrains, seen in previous work on the deposition of nickel alloys using ESD. Ebrahimnia et al. (2014) identified these subgrains are being composed of primary dendrite cells with no secondary dendrite structures, comparable to that identified by Savage et al. (1976) as occurring during cellular dendritic solidification modes in copper-nickel alloys. This and other work on solidification modes is summarized by Lippold (2015), who states that the cellular dendritic subgrain structure is a result of both high temperature gradients in the liquid and high solidification growth rates.

These cellular dendritic subgrain structures are predicted to form epitaxially with the rapid solidification of the deposited layer, where initial subgrain formation starts at the interface of the previous layer or substrate and propagates towards the deposition surface. Fig. 2 shows that grain formation is influenced by the substrate grain structure; grain boundaries extend across the substrate-deposition interface, with the structure changing from equiaxed in the substrate to epitaxial in the deposition. Electron backscatter diffraction (EBSD) techniques used by Ebrahimnia et al. (2014) for an ESD Inconel 738LC deposition identify splats with sufficient fusion to the substrate as having cellular growth in the same crystallographic orientation as substrate grains. However, the presence of impurities and lack of fusion defects can result in misoriented cellular growth.

In an analysis of columnar to equiaxed transition in solidification processes, Kurz et al. (2001) concluded that the solidification of molten material typically leads to equiaxed grains when local heat flux is equal in all directions and epitaxial grains when local heat flux occurs preferentially in one direction. The change in morphology can therefore be attributed to unidirectional heat flux within the deposited layers during ESD, compared to the uniform heat flux experienced by the substrate during its subgrain formation. Fig. 3 shows cellular dendritic subgrains of approximately 800 nm in diameter, surrounded by splats with thinner or no discernable subgrain structure. Larger cellular subgrains are visible in etched samples with the use of an optical microscope, as seen in Fig. 3c and d. These images more clearly show the existence of competing cellular subgrain growth directions. Although a majority grow with small angles to the vertical direction – which matches the direction of heat flow – some growth occurs at almost 90° to the vertical direction.

During ESD, the cellular subgrains form at the solid-liquid interface as the deposited splat cools below its melting point and the solid-liquid interface moves from the substrate-deposition interface towards the deposition surface. As the solidified material continues to cool, the fine cellular structure is expected to undergo coarsening. The amount of coarsening depends on the amount of time the solidified deposition remains at an elevated temperature. In Fig. 3, it is possible to distinguish the difference in cellular dendritic subgrain diameters between the individual deposition splats. The subgrain diameter is defined as starting at the inner leftmost edge of a subgrain and extending to the inner leftmost edge of the adjacent subgrain (Fig. 2), and is calculated using the intercept method as described in the experimental section. Arrow 2 indicates a region with fine cellular structures when compared to the thick deposition splat and thicker cellular structures indicated by arrow 1. The presence of larger diameter subgrains in thicker splats suggests that the thickness of material deposited with each pulse in the ESD process is correlated to the final microstructure.

This premise stems from the larger time requirement for cooling thicker deposition splats. The longer duration at elevated temperatures is expected to act as the mechanism that induces coarsening, resulting in larger cellular dendritic subgrain diameters for thicker splats. This type of subgrain coarsening has been shown to follow the subgrain growth equation (Rollett et al.. 2004),

$$d^n = k_T t + d_0^n \quad (1)$$

where d is the final subgrain diameter, k_T is a temperature dependent rate constant, d_0 is the initial subgrain diameter, t is the time, and the

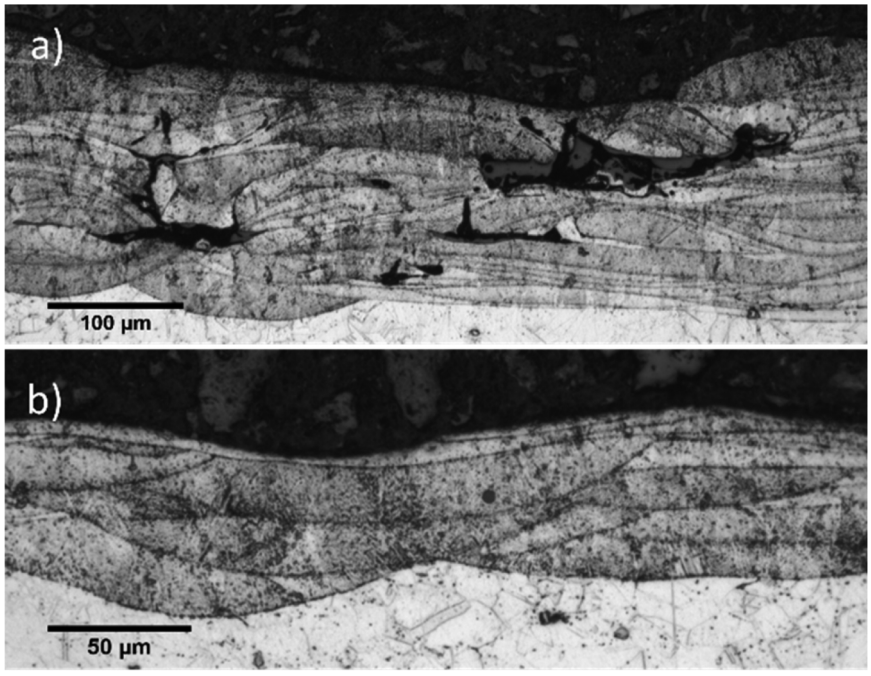

Fig. 1. OM image of **a)** 120 V, 120 µF, 170 Hz ESD deposition and **b)** 100 V, 80 µF, 170 Hz ESD deposition.

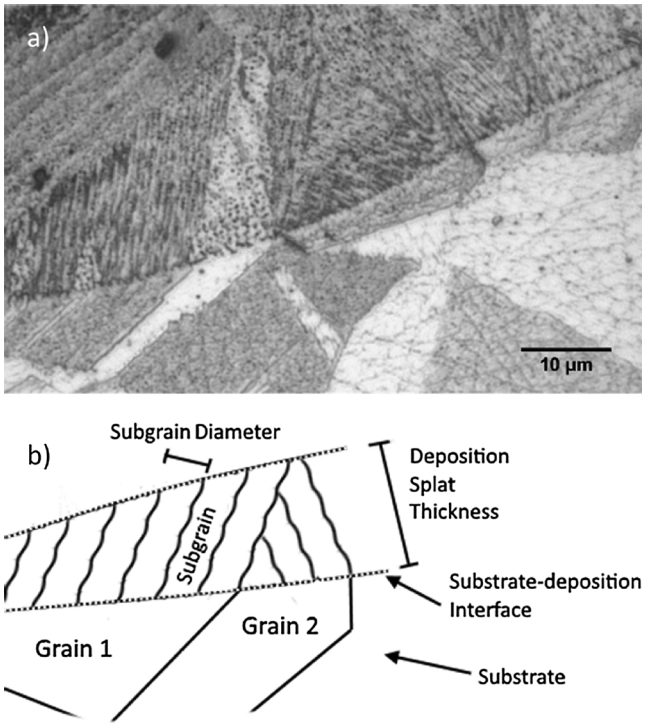

Fig. 2. a) OM image along substrate-deposition interface and **b)** schematic of competitive cellular dendritic subgrain growth directions at the interface.

growth exponent n has a theoretical value of 2 when derived using a boundary migration model in a pure single-phase system. Brook (1976) proposed that n ranges between ideal values of 1 and 4 depending on several factors including the presence of impurities in single phase systems, the continuity and mobility of secondary phases, and the diffusion mechanism responsible for boundary mobility. Similarly, k_T is derived from an Arrhenius-type equation that depends on the activation energy of the grain growth mechanism, which – typically irrespective of grain size – is more commonly boundary diffusion than lattice diffusion (Koch and Suryanarayana, 2000).

As previously stated, the subgrain growth process for ESD is expected to begin with a short-lived nucleation stage during the rapid solidification process. The starting diameter of these cellular dendritic subgrains is assumed negligible in comparison to the final diameter, simplifying Eq. (1) by setting d_0 to zero as was proposed by Martin et al. (1997). A simple relationship now exists between the subgrain diameter and the coarsening time,

$$d = \sqrt[n]{k_T t} \tag{2}$$

Accurate experimental measurements of cooling time for each deposition are not easily made, requiring that a relationship be developed between the deposition splat thickness and cooling time. This relationship can be developed through an analysis of the heat diffusion equation, which can be simplified to one dimension, as heat can be assumed to transfer from the deposition to the substrate in the vertical axis. Eq. (3) presents the one-dimensional form of the heat diffusion equation,

$$\frac{\partial T}{\partial t} = \frac{k}{c_p \rho}\left(\frac{\partial^2 T}{\partial x^2}\right) \tag{3}$$

where T is the temperature, t is the time, k is the thermal conductivity of Inconel 718 (11.4 $\mathrm{W\,m^{-1}\,K^{-1}}$ (MatWeb, 2017)), c_p is the specific heat capacity of Inconel 718 (0.435 $\mathrm{J\,g^{-1}\,K^{-1}}$ (MatWeb, 2017)), ρ is the mass density of Inconel 718 (8.19 $\mathrm{g\,cm^{-3}}$ (MatWeb, 2017)), and x is distance in the vertical axis. Further assumptions can be made when modeling heat diffusion within this system; the size of the substrate allows it to act as an infinite heat sink while maintaining the starting room temperature and the argon atmosphere above the deposition has no ability to remove heat from the deposited material. This results in one Dirichlet boundary condition at the substrate and one Neumann boundary condition at the argon-deposition interface, as shown in Eq. (4).

$$T = 298.15,\ \frac{\partial T}{\partial t} = 0 \tag{4}$$

Additionally, since subgrain coarsening begins once the deposition has solidified, the initial temperature is approximated as the solidus temperature for Inconel 718 (1533.15 K (MatWeb, 2017)). These

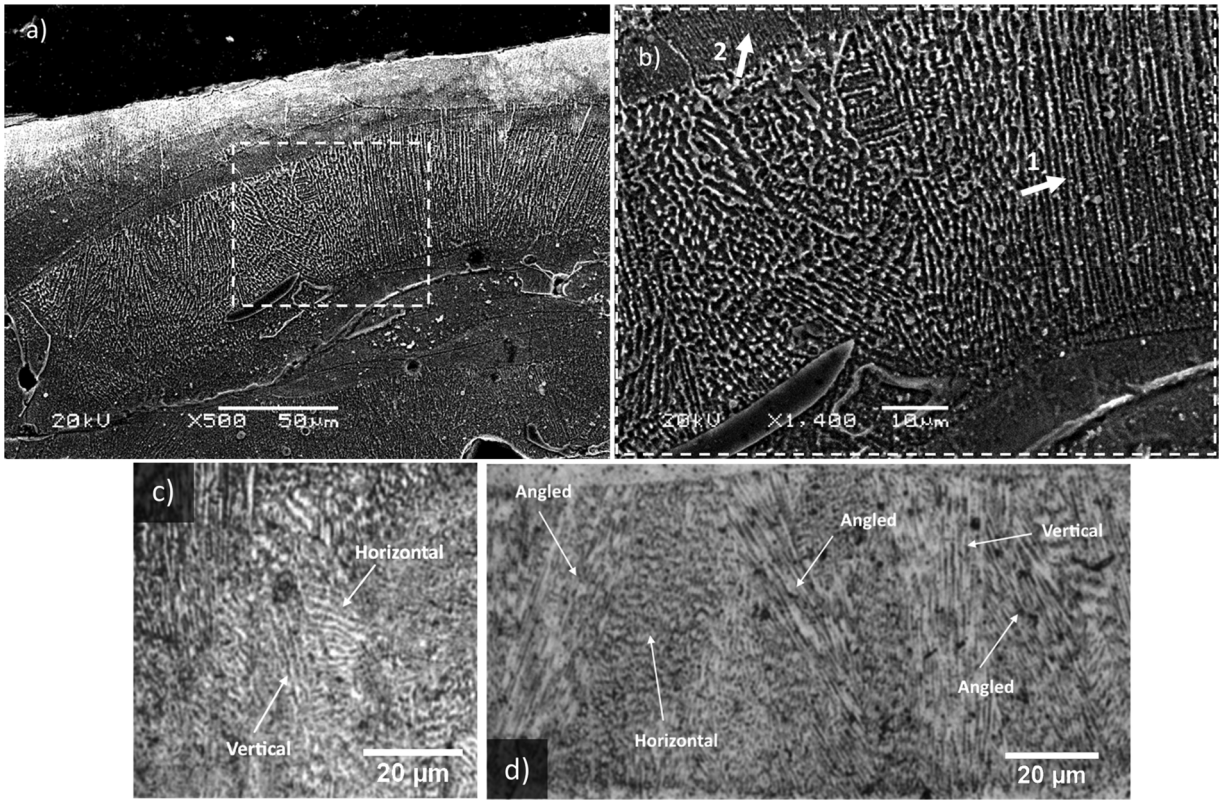

Fig. 3. a) SEM image of deposition with cellular dendritic subgrain, **b)** area of interest, and OM images of competing cellular growth directions in **c)** a 100 µm thick splat and **d)** a 70 µm thick splat.

assumptions allow for the solution of the heat diffusion equation using the method of lines technique for partial differential equations. The spatial dimensions in Eq. (3) are discretized using centered finite difference and the resulting ordinary differential equation (Eq. (5)) is solved numerically using MATLAB's ode45 built-in function to find the temperature profile as the cooling process progresses.

$$\frac{\partial T}{\partial t} = \frac{k}{c_p \rho}\left(\frac{T_{i+1} - 2T_i + T_{i-1}}{(\Delta x)^2}\right) \tag{5}$$

For a 10 and 20 µm thick deposition splat, the temperature profile throughout the material is shown as it progresses over time in Fig. 4. As can be seen by the diverging temperature profiles, a longer period of time is required to cool depositions with larger thicknesses.

To determine the effect of deposition thickness (L) on the time required to cool the deposition to the substrate temperature, the average temperature at each time step is calculated (Eq. (6)) using MATLAB's trapz built-in function.

$$T_{avg} = \frac{1}{L}\int_0^L T\partial x \tag{6}$$

The time required to reach an average deposition splat temperature within 1 K of the substrate is calculated for depositions between 5 µm and 30 µm thick, with the results shown in Fig. 5.

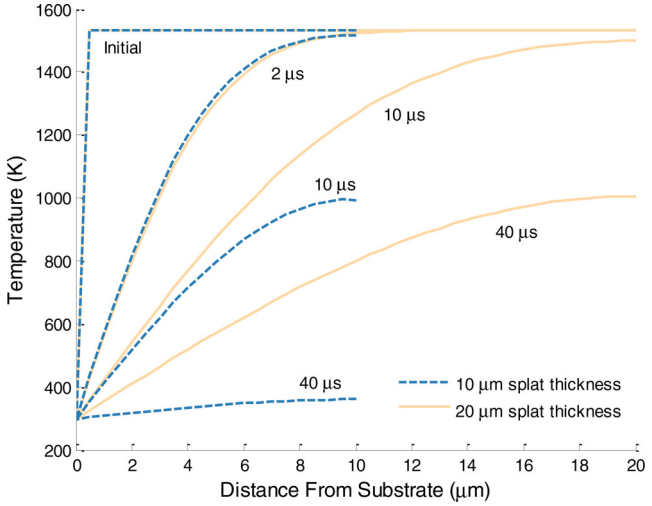

Fig. 4. Temperature profile of 10 and 20 µm thick deposition splat during cooling process.

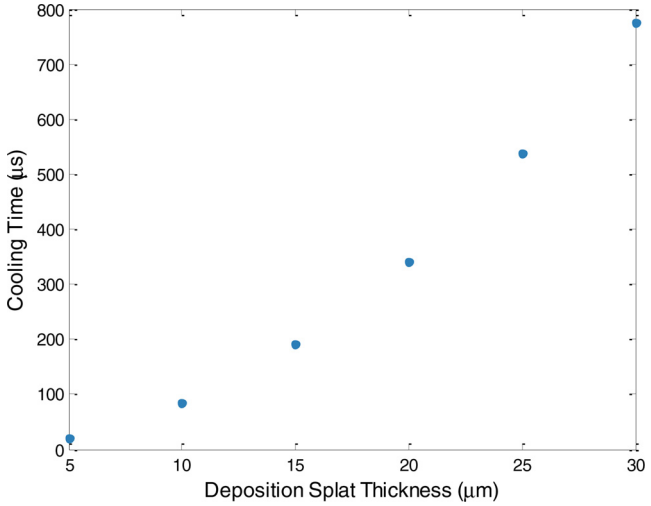

Fig. 5. Time required to cool a deposition splat to an average temperature of 299.15 K.

An analysis of the solution shows a square dependence between the time required to reduce the temperature of a deposition and its thickness,

$$t = \beta x^2 \tag{7}$$

related by a constant β. Varying the initial condition (temperature), substrate temperature or material dependent constants (k, c_p and ρ) result in changes to the value of β while maintaining the square relation between time and thickness. Substituting this relationship into Eq. (2) results in,

$$d = Cx^{2/n} \tag{8}$$

where C is equal to $\sqrt[n]{k_T\beta}$. The dependence of the final subgrain diameter on constants n and C (which includes both n and k_T) suggest a significant influence of the grain growth mechanism on the amount of coarsening experienced during the cooling of an ESD splat. Another influence on subgrain growth can be attributed to temperature and material properties such as density, specific heat capacity and thermal conductivity through the constant C, which is influenced by β.

Eq. (8) provides a model by which to analyze experimental values. Experimental cellular dendritic subgrain diameters and the respective deposition splat thicknesses are displayed in Fig. 6. The sample size used for the analysis consisted of 728 cellular dendritic subgrains – examples of which are shown in Fig. 3 – and were measured using the intercept method described in the experimental methods section. Table 3 contains the best fit parameters for an exponential relationship, as well as the R^2 and normalized root-mean-square error values for the model.

For the current system, Eq. (8) is able to relate the thickness of a deposition splat made by ESD to the diameter of the resulting cellular dendritic subgrains with relatively high accuracy, as shown with the R^2 value in Table 3. The process dependence of deposition splat thickness, in which higher energy parameters result in greater material transfer and thicker splats, indicates that a reduction in energy input during ESD results in splats with finer subgrain structures. The exponent n is found to vary from the ideally predicted value of 2, although it is still similar to previously reported experimental results for the subgrain growth equation (Rollett et al., 2004). Based on a derivation by Brook (1976), a fit parameter n of approximately 4 suggests the presence of an impure system in which the grain growth mechanism occurs through the coalescence of a secondary (in this case interdendritic) phase by boundary diffusion. ESD processed materials have been shown by Ebrahimnia et al. (2014) to exhibit interdendritic secondary phases, which can be expected to coalesce during the subgrain coarsening process. The effect

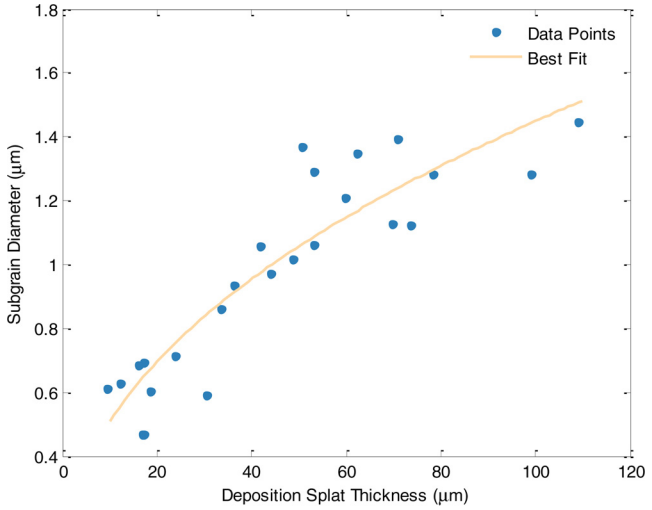

Fig. 6. Average cellular dendritic subgrain size for various deposition splat thicknesses.

Table 3
Fit parameters for subgrain size and deposition thickness relationship.

	Fit Parameters		Model Summary	
Form	C	n	R^2	NRMSE
Eq. (8)	0.178	4.387	0.82	0.14

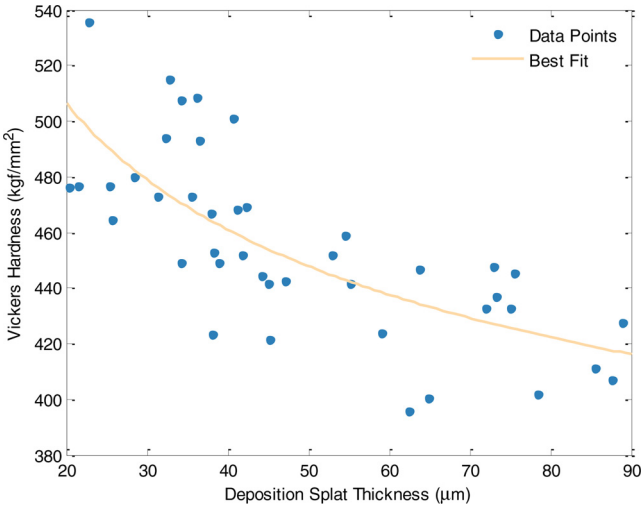

Fig. 7. Vickers hardness for various deposition splat thicknesses.

Table 4
Fit parameters for deposition splat thickness and Vickers hardness.

	Fit Parameters		Model Summary	
Form	HV_0	k	R^2	NRMSE
Eq. (10)	195.742	259.096	0.53	0.16

of grain growth mechanism on n and C suggests that they are highly material dependent parameters. However, the dependence of C on β, which partly depends on the temperature differential between the substrate and deposited material, suggests that substrate temperature is another process parameter (in addition to energy input) that can affect the final subgrain diameter.

Contrary to the assumptions made in Eqs. (3) and (4), some heat loss is expected at the argon-deposition interface, and not all heat transfer occurs only in the x-axis. Some heat may be removed from the deposited layer in a direction with components perpendicular to the x-axis, as suggested by competing growth directions of the cellular subgrains. Additionally, the temperature profile in a deposited material is not uniform over time; a longer exposure to higher temperatures further from the substrate surface leads to some variations in subgrain coarsening within a deposition. These non-idealities are likely to introduce deviations from the model – particularly for thicker depositions – which helps to explain the non-ideal R^2 value. Additionally, very thick splats beyond those studied here are expected to experience a cellular to equiaxed transition. As the solidification front moves through thicker depositions, decreasing thermal gradients and increasing solidification velocities may result in morphological changes that make comparisons between subgrain diameters in thin and thick deposition splats inaccurate. The model fit parameters presented in Table 3 may not be applicable to this scenario and should be taken into consideration before extending the model to larger splat thicknesses.

The relationship between deposition splat thickness and subgrain diameter can be extended to explain the mechanical properties of the deposited material. The Vickers hardness (HV) can be related to grain size using a relationship analogous to the Hall-Petch equation, previously applied by Hanamura and Qiu (2014) to investigate the

hardness of steels in relation to their grain size. This expression is shown in Eq. (9),

$$HV = HV_0 + kd^{-1/2} \quad (9)$$

where HV_0 and k are fitted constants and the Hall-Petch relationship is extended to subgrain diameter (d) as suggested by (Rollett et al., 2004). Substitution of the relationship between subgrain diameter and deposition splat thickness (Eq. (8)) into Eq. (9) results in a relationship between the Vickers hardness and the thickness of the deposition splat,

$$HV = HV_0 + kC^{-1/2}x^{-1/n} \quad (10)$$

with the values of C and n previously listed in Table 3. HV_0 is analogous to the friction stress constant in a traditional Hall-Petch relationship, which is indicative of the lattice's intrinsic resistance to dislocation motion. The strengthening coefficient k is described by Russell and Lee (2005) as the stress intensity required to induce plastic yielding across grain boundaries, which is expected to extend to subgrain boundaries as well. Hardness and splat thickness data obtained from ESD processed samples are shown in Fig. 7, along with best fit parameters in Table 4 for the relationship in Eq. (10).

Due to the nature of microhardness measurements there exists significant variation in the gathered data, as shown by the lower R^2 value. EDX measurements show negligible differences in composition between areas measured at similar deposition splat thicknesses. Therefore, variation in the hardness values can likely be attributed to other material properties including variations in subgrain orientation and surface texture, as suggested by the relevant testing standards (ASTM E384-16). Resistance to deformation is highly dependent on cellular dendritic subgrain orientation, with some orientations providing greater or lower resistance than others. This effect is more prevalent when small indentation sizes are used, since dendritic subgrains in contact with the indenter may be uniformly oriented in high or low resistance orientations. However, the results still indicate the existence of a negative relationship between deposition hardness and splat thickness. As indicated by Russell and Lee (2005), larger spacing between boundaries provides less barriers to dislocation movement and lower strength. This larger spacing is a result of subgrain coarsening that occurs to a greater extent in thicker deposition splats, resulting in lower Vickers hardness. Through the models presented in Eqs. (8) and (10), it has been demonstrated that the deposition splat thickness can be used to predict cellular dendritic subgrain size and deposited material properties. Improved performance of ESD processed materials is obtained with the use of lower energy input, which results in less material transfer, thinner deposition splats, finer subgrain features and higher hardness.

4. Conclusions

The use of lower energy input during ESD to achieve thinner deposition splats results in improved coating quality, finer subgrain size and improved mechanical properties.

- Thinner deposition splats result in smaller diameter cellular dendritic subgrains. This is due to higher cooling rates and a smaller degree of coarsening after the solidification of the molten deposition.
- Material within thinner deposition splats show higher microhardness as a result of the finer subgrain structure in accordance with a Hall-Petch relationship.

Acknowledgements

This work was performed with funding support from the Natural Sciences and Engineering Research Council of Canada (NSERC), the Canada Research Chairs (CRC) Program and Huys Industries, in collaboration with the Centre for Advanced Materials Joining and the Multi-Scale Additive Manufacturing Lab at the University of Waterloo.

References

Brochu, M., Portillo, G., 2013. Grain refinement during rapid solidification of aluminum-zirconium alloys using electrospark deposition. Mater. Trans. 54, 934–939. http://dx.doi.org/10.2320/matertrans.MD201228.

Brook, R.J., 1976. Controlled grain growth. Ceramic Fabrication Processes: Treatise Mater. Sci. Technol. pp. 331–364. http://dx.doi.org/10.1016/B978-0-12-341809-8.50024-3.

Ebrahimnia, M., Malek Ghaini, F., Xie, Y.J., Shahverdi, H., 2014. Microstructural characteristics of the built up layer of a precipitation hardened nickel based superalloy by electrospark deposition. Surf. Coat. Technol. 258, 515–523. http://dx.doi.org/10.1016/j.surfcoat.2014.08.045.

Farhat, R., Brochu, M., 2012. Utilisation of electrospark deposition to restore local oxidation resistance properties in damaged NiCoCrAlY and CoNiCrAlY coatings. Can. Metall. Q. 51, 313–319. http://dx.doi.org/10.1179/1879139512Y.0000000019.

Hanamura, T., Qiu, H., 2014. Analysis of Fracture Toughness Mechanism in Ultra-fine-grained Steels, NIMS Monographs. Springer, Japan, Tokyo. http://dx.doi.org/10.1007/978-4-431-54499-9.

Koch, C.C., Suryanarayana, C., 2000. Nanocrystalline materials. Microstruct. Prop. Mater. WORLD SCIENTIFIC. pp. 359–403. http://dx.doi.org/10.1142/9789812793959_0006.

Kurz, W., Bezençon, C., Gäumann, M., 2001. Columnar to equiaxed transition in solidification processing. Sci. Technol. Adv. Mater. 2, 185–191. http://dx.doi.org/10.1016/S1468-6996(01)00047-X.

Lippold, J.C., 2015. Welding Metallurgy and Weldability. John Wiley & Sons, Inc, Hoboken, New Jersey.

Martin, J.W., Doherty, R.D., Cantor, B., 1997. Stability of Microstructure in Metallic Systems. Cambridge University Press.

MatWeb, 2017. Special Metals INCONEL Alloy 718 [WWW Document]. (Accessed 13 June 17). http://www.matweb.com.

Rollett, A., Humphreys, F., Rohrer, G., Hatherly, M., 2004. Recrystallisation and Related Annealing Phenomena, 2nd ed. Elsevier.

Ruan, Y., Mohajerani, A., Dao, M., 2016. Microstructural and mechanical-property manipulation through rapid dendrite growth and undercooling in an Fe-based multinary alloy. Sci. Rep. 6, 1–11. http://dx.doi.org/10.1038/srep31684.

Russell, A.M., Lee, K.L., 2005. Structure-Property Relations in Nonferrous Metals. John Wiley & Sons.

Saarimäki, J., Lundberg, M., Moverare, J.J., Brodin, H., 2016. Characterization of Hastelloy X Produced by Laser Powder Bed Additive Manufacturing. World PM2016. 1–6.

Sartwell, B.D., Legg, K.O., Price, N., Aylor, D., Champagne, V., Pepi, M., Pollard, T., 2006. Electrospark deposition for depot- and field-level component repair and replacement of hard chromium plating. Environ. Secur. Technol. Certif. Progr. 299.

Savage, W.F., Nippes, E.F., Miller, T.W., 1976. Microsegregation in 70Cu-30Ni weld metal. Weld. J. 165s–173s.

Vander Voort, G.F., 1998. Metallographic Technique for Nonferrous Metals and Special-Purpose Alloys, Met. Handb. ASM International.

Wang, J., Meng, H., Yu, H., Fan, Z., Sun, D., 2010. Wear characteristics of spheroidal graphite roll WC-8Co coating produced by electro-spark deposition. Rare Met. 29, 174–179. http://dx.doi.org/10.1007/s12598-010-0030-6.

Wei, X., Chen, Z., Zhong, J., Wang, L., Hou, Z., Zhang, Y., Tan, F., 2017. Facile preparation of nanocrystalline Fe2B coating by direct electro-spark deposition of coarse-grained Fe2B electrode material. J. Alloys Compd. 717, 31–40. http://dx.doi.org/10.1016/j.jallcom.2017.05.081.